New Journal and we have not received input yet 25 (2021) 100993

Contents lists available at ScienceDirect

Thermal Science and Engineering Progress

journal homepage: www.sciencedirect.com/journal/thermal-science-and-engineering-progress

A comprehensive numerical investigation of unsteady-state two-phase flow in gravity assisted heat pipe enclosure

Halit Arat [a], Oguz Arslan [b], Umran Ercetin [a], Abdullah Akbulut [a]

[a] Mechanical Engineering Department, Kutahya Dumlupinar University Engineering Faculty, 43270 Kutahya, Turkey
[b] Mechanical Engineering Department, Bilecik Seyh Edebali University Engineering Faculty, 11230 Bilecik, Turkey

ARTICLE INFO

Keywords:
Thermosyphon
CFD
Combined numerical model
Turbulence models
Thermal performance
Two-phase flow
Heat transfer coefficient

ABSTRACT

In this study, thermal performance analysis of glass and copper two-phase closed thermosyphons (*TPCTs*) were investigated as *3D* using comprehensive experimental methods and a new combined numerical model containing two stages. For this purpose, Volume of Fluid model has been used for the first 60 s, and Eulerian model has been employed after 60 s until 180 s for the first time in the literature. For the verification of this numerical analysis, the surface temperatures of *TPCTs* were measured at twenty different points by K-type thermocouples. The pressure change inside the pipes was measured by a vacuum manometer. A video camera was utilized to observe the change of steam and water volumes in the glass *TPCT*. The experimental and numerical results were also compared with each other in real-time for the first time in the literature. According to results, the numerical temperature distributions and steam volumes in *TPCTs* have shown a similar trend with the studies in the literature. It was observed that the maximum absolute temperature difference values in the evaporation, middle and condenser regions for *TPCTs* ranged from 6.81 K to 18.63 K. These values are similar to the values in the other studies. The maximum absolute temperature difference values were calculated between 12.09 K and 26.07 K for different turbulence models.

1. Introduction

In recent days, energy usage has increased because of developing technology and the rising population. All countries should utilize their limited energy efficiently to meet this enormous energy demand. For this purpose, heating systems like two-phase closed thermosyphons (*TPCTs*) providing efficient heat transfer with phase transition between interfaces have started widely use nowadays [1–4].

There are some different methods to simulate two-phase problems. In order to balance mass, momentum, and energy at the interface, the phase change models have mostly enforce additional source terms in the governing equations [5]. Schrage model is based on the Hertz-Knudsen equation to calculate the net mass transfer rate per unit area through the interface, enabling the interface temperature and pressure to jump across the interface [6]. Besides, Lee model is one of the most accepted phase change mass transfers. It is mainly driven by the deviation between the interface temperature and the saturation temperature, and the phase change rate is proportional to the deviation [7]. Moreover, Nichita and Thome [8], integrated the level set approach in FLUENT and combined it with the existing volume of fluid method to simulate two-phase flow. In addition, they also applied phase change heat transfer.

The *TPCT* consists of three main parts that are adiabatic, evaporating, and condensing sections. When the fluid inside the *TPCT* is heated, it boils and evaporates ascending to the top of the *TPCT* at a constant temperature. At this point, the rising steam begins to condensate, and two-phase flow occurs inside the heat pipe. According to the literature, the mechanism playing a primary role in the two-phase flow is one of the most economical and practical methods [9–16]. In this way, energy could be utilized more efficiently.

Numerical studies compared with the experimental studies provide more quick and cheap solutions in many valuable works to the academicians. There are many experimental and numerical studies about the evaporation–condensation in wicked or wickless heat pipe in the literature. To simulate the heat pipe as numerical, the authors have to use multiphase model in the computational fluid dynamic programs like Ansys Fluent. The researchers who model the numerical heat pipe can select the three multiphase models (Eulerian, Mixture, and Volume of Fluid) in Fluent database. In this study, Eulerian and Volume of Fluid (*VOF*) multiphase models were performed. Eulerian multiphase model is a multi-fluid model with single-phase and interfacial terms in the conservation equations for each phase individually [17]. *VOF* model which

E-mail addresses: halit.arat@dpu.edu.tr (H. Arat), oguz.arslan@bilecik.edu.tr (O. Arslan), umran.ercetin@dpu.edu.tr (U. Ercetin), abdullah.akbulut@dpu.edu.tr (A. Akbulut).

https://doi.org/10.1016/j.tsep.2021.100993
Received 6 May 2021; Received in revised form 9 June 2021; Accepted 10 June 2021
Available online 15 June 2021

Nomenclature

α	The volume fraction (0–1)
cov	The coefficient of variation
E	Energy (kJ/s)
ε	Dissipation rate
$\overrightarrow{F}_{st}$	The surface tension force (N)
$\overrightarrow{g}$	Gravity acceleration (m/s^2)
$\overline{h}_{air,L_{cooling}}$	The heat transfer coefficient of air around the cooling region (W/m^{2}K)
$\overline{h}_{water,L_{heating}}$	The heat transfer coefficient of water around the heating region (W/m^{2}K)
k	Thermal conductivity (W/m.K)
κ	The surface curvature (m^{-1})
L_{cond}	The length of the condensation region (m)
$L_{cooling}$	The length of the cooling region (m)
L_{evap}	The length of the evaporation region (m)
$L_{heating}$	The length of the heating region (m)
L_{mid}	The length of the middle region (m)
MPE	The mean percentage error
$\dot{m}_{ba}$	The mass transfer from phase b to phase a (kg/s)
$\dot{m}_{ab}$	The mass transfer from phase a to phase b (kg/s)
μ	Dynamic viscosity (Pa.s)
n	The numbers of the measurement
Nu	Nusselt number (-)
P	Pressure (kPa)
Pr	Prandtl number (-)
$\dot{Q}_{cooling}$	The heat transferred to ambient from cooling region (W)
$\dot{Q}_{heating}$	The heat transferred to the heating region from the heat source (W)
R	Thermal resistance (K/W)
Ra	Rayleigh number (−)
$RMSE$	The error of the square root
R^2	The percentage of absolute change
ρ	Density (kg/m^3)
σ	The surface tension coefficient (N.m^{-1})
SD	Standard deviation
t	Time (s)
T	Temperature (K)
T_{amb}	The temperatures of ambient (K)
T_{CFD}	The numerical temperature value (K)
$T_{cond,ave}$	The average temperature of the condensation region (K)
$T_{evap,ave}$	The average temperature of the evaporation region (K)
T_{EXP}	The experimental temperature value (K)
T_{heat}	The temperatures of the heat source (K)
$T_{mid,ave}$	The average temperature of the middle region (K)
$T_{s,cooling}$	The temperatures of condensation surface (K)
$T_{s,heating}$	The temperatures of the heating surface (K)
ΔT	The temperature difference (K)
U	Uncertainty (±K or ±kPa)
V	Velocity (m/s)
X_m	The measured value
$\overline{X}$	The average of the measured values
y_{output}	The output value
$\overline{y}_{output}$	The average output value
y_{actual}	The actual value
$\overline{y}_{actual}$	The average actual value

tracks the location and motion of a free surface between two or more immiscible fluids relies on the fact that two or more phases do not penetrate each other, and for each additional phase, the volume fraction of that phase must be added to the calculation [18]. Because the difference in void fraction prediction is minimal in bubbly flow, the Euler model is more accurate than the *VOF* model, and both models have difficulties simulating annular flow. The accuracy of the model can be improved by combining new *CFD* models. *VOF* model, on the other hand, can identify the discontinuous and continuous phases in the solution appearance, in contrast to the Eulerian model [19]. Moreover, the mass transfer coefficient is one of the crucial parameters to simulate the evaporation and condensation mechanism in Lee model which is used both Eulerian and *VOF* multiphase models. In order to get the least difference between experimental and numerical results, researchers in the literature have employed a wide range of values, ranging from 0.1 to 1×10^{-7} s^{-1} [7]. In the literature, the mass transfer coefficients were generally applied as 0.1 s^{-1} to simulate boiling process at the atmospheric pressure [20,21]. Zang et al. [22], have investigated the boiling flow of R141B in a horizontal coiled tube by using the *VOF* multiphase flow model with the mass transfer coefficients of 100 s^{-1} while Gorlé et al. [23], have performed the conjugate heat transfer *VOF* simulations with three different mass transfer coefficients (500, 1000, and 5000 s^{-1}) for two-phase cooling in a micro-channel.

Venkata and Bhramara [24] have investigated two-phase flow in pulsating heat pipe using methanol as working fluid by utilizing computational fluid dynamic (*CFD*) software ANSYS. They selected a temperature of 302 K and heat flux of 4423 W/m^2 as boundary conditions in the condenser and evaporator region, respectively. Besides, in the adiabatic region, boundary condition defines as heat flux of 0 W/m^2. As a result, they obtained that thermal resistance decreases, and the heat transfer coefficient increases with the increase in heat flux.

Sarmasti Emami et al. [25] have experimentally investigated the geyser boiling phenomenon in a two-phase closed thermosyphon, considering the effects of inclination angle, filling ratio, and input heat rate, the mass flow rate of coolant, and inside diameter of the tube. They used three copper thermosyphons with inside diameters of 14 mm, 20 mm, and 24 mm with a length of 1000 mm and employed the distilled water as working fluid in thermosyphons. Their results showed that the filling ratio should be less than 30% to prevent the geyser-boiling phenomenon, and the impact intensity applied to the end cap of the evaporator was reduced by reducing the inclination angle to a value below 15°. Also, the coolant mass flow rate in the condenser jacket does not affect this phenomenon's behavior.

Zhang et al. [26] constructed a heat pipe flat-plate solar collector model based on the finite volume method and numerically simulated it under steady-state conditions. Also, they investigated the effect of pipe diameter, evaporator length, and inclination angle on solar collector efficiency. The results showed that pipe diameter of 12 mm, inclination angle between 30° and 45°, and decreasing evaporator length help increase instantaneous efficiency.

Xia et al. [27] have experimentally studied phase-change instabilities in a flat two-phase closed evaporator and condenser coexisting system with three working fluids (water, ethanol, and acetone) under subatmospheric pressures and to visualize phase change processes with a high-speed camera to understand mechanisms. While the test section's internal chamber has a diameter of 80 mm and a height of 60 mm, they used a quartz tube with an outside diameter of 90 mm, a thickness of 5 mm, and a height of 40 mm to observe the heat transfer process. As a result, the maximum intensity of fluctuations of evaporator wall temperature and vapor pressures were 3.1°C and 0.8 kPa for distilled water as working fluid at a filling ratio of 50% and the temperature of inlet cooling water of 12°C. Besides, they showed that the heat transfer mode for ethanol and acetone was mainly nucleation boiling and fully developed regimes, and heat transfer was steady.

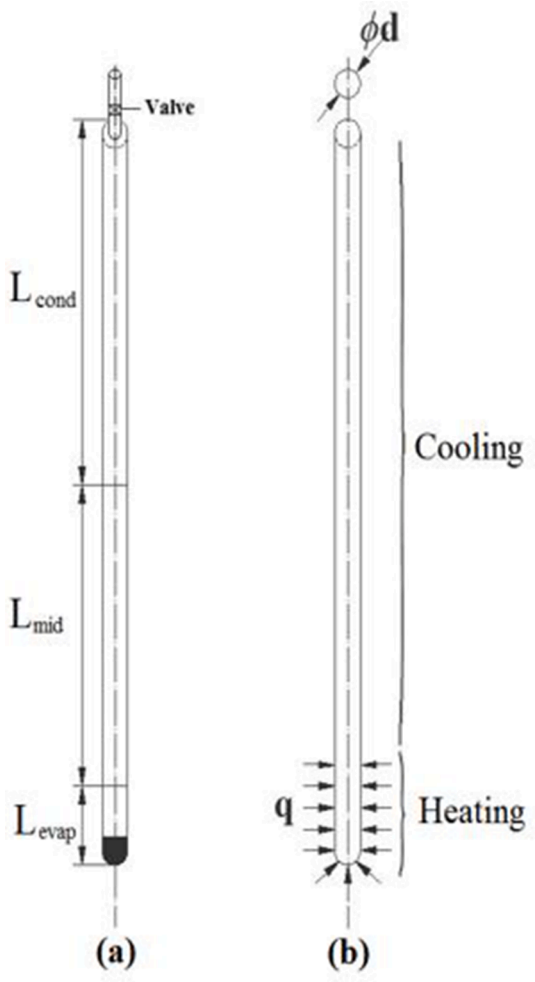

Fig. 1. The schematic of the vertical copper and glass *TPCTs* and the regions in that.

Venkata and Bhramara [28] have numerically analyzed closed-loop *U*-pipe by using *CFD* software ANSYS. They have utilized water-methanol and water–ethanol as working fluid in half of *U*-pipe geometry. They defined the heating power of 10 W to 70 W and the heat flux of -1000 W/m^2 as a boundary condition in the evaporator and condenser region. Besides, the boundary condition defines as heat flux of 0 W/m^2 in the adiabatic region. Also, they selected the Volume of Fluid (*VOF*) model as the multiphase model and *k*-ε as the turbulence model. When their obtained *CFD* results are compared to their experimental study, they observed that the minimum deviations in thermal resistance values are between 6% and 30%.

Smith et al. [29] investigated flow and boiling regimes occurring within transparent thermosyphon of a small diameter of 8 mm. This system composed of the length of evaporator, condenser, and adiabatic sections was 100 mm, 200 mm, and 180 mm, respectively. They found out that flow is characterized as slug/plug flow for high levels of confinement and low rates of vapor production and nucleate pool boiling regimes present in the evaporator at low vapor production rates unconfined flows. Especially at low operating pressures, geyser boiling is a prominent behavior for water and ethanol because of high surface tension and high vapor specific volume, leading to high levels of confinement and high superficial vapor velocities.

Wang et al. [30] have investigated a combined *CFD*/visualization of heat transfer behaviors to promote the understanding of geyser boiling in two-phase closed thermosyphon modeling as *2D* geometry composed of the inside diameter of 15 mm and length of the evaporator (Boundary Conditions-*BC*:360.8 K/913.2 W/m^{2}K), condenser (*BC*:302.4 K/682 W/m^{2}K), and adiabatic (*BC*:0 W/m^2) sections were 160 mm, 100 mm, and 180 mm respectively. The results showed that the improved model's heat transfer behaviors were closer to the actual phenomenon in visualization test, slug bubble growth, and flowing-up liquid phenomenon. Besides, heat transfer behaviors, such as surface evaporation and thermally natural convection of liquid pool, and evaporation of returning droplets during the incubation period were also better prediction performance of this improved phase change model.

According to the previous studies in the literature, the numerical simulations have usually been performed by using *2D* geometry instead of the rare *3D* [31] modeling. Besides, previous simulations assumed that *TPCT* filled water and steam; however, it filled water with the air space, and there was no steam at the beginning of the simulation. The steam volume starts to occur after the temperature of that reaching saturation temperature as in reality. Also, the diameter and length of the *TPCT* were usually used in the small dimensions relatively. In this study, a comprehensive experimental and numerical study was performed for the glass and copper *TPCT's* thermal performance analysis in detail. For this purpose, a new combined numerical model composed of two stages that were *VOF* and Eulerian multiphase models for the *TPCT* was performed as *3D* and analyzed thermodynamically for the first time in the literature. While the *TPCT*'s evaporation region is filled with the water liquid of 10 ml, the other regions are filled with the air at a low density. *k*–ε turbulence model, which is used in the most general multiphase turbulence, was applied in both *VOF* and *Eulerian* multiphase models.

Nevertheless, different turbulence models like *LES*, *k-kl* ω transition, *k-ω*, *SAS*, and *Re-Stress* with *k*–ε were examined in *VOF* which have more turbulence options than Eulerian for comparing them. For the verification of this numerical analysis, the experimental study was performed by vacuuming the glass and copper pipes up to 6 kPa and immersing them in a heat source at a constant temperature of 355 K. The *TPCTs'* surface temperatures were measured at twenty different points using K-type thermocouples. The change of the pressure inside the pipes was measured using an analog vacuum manometer. The experimental and numerical results were compared with each other in real-time steps for the first time in the literature. Although the primary purpose of this study is to analyze the copper *TPCT* numerically, a video camera was utilized to observe the change of the steam and water volumes in the glass *TPCT*. Therefore, the glass *TPCT* was used for observing the boiling process in the pipe.

2. Materials & method

2.1. Vertical TPCT design

The *TPCT* was designed as a circular closed tube system, and single or two-phase flow heat transfer mechanisms were numerically modeled in cases such as boiling, evaporation, and condensation. The schematic of the vertical copper and glass *TPCTs* and the regions were given in Fig. 1.

According to Fig. 1a, the *TPCT* consists of three different regions; at the bottom is the evaporation region indicated by L_{evap}. L_{mid} is the middle region in between evaporation and condensation regions, and the condensation region is indicated by L_{cond}. The valve located at the top of the *TPCT* connects the pipe and vacuum pump and controls the filling water liquid inside a *TPCT*. The evaporation region is the circular closed tube section that is filled with water liquid from the bottom to a certain height. According to Fig. 1b, the zone where the heat flux of *q* defined on the outer wall is the heating region with a 100 mm long section from the bottom of the *TPCT*. Also, the pipe surface above the heating region is defined as the cooling region. The water liquid at the bottom of the pipe begins to evaporate and runs into the middle region when the *TPCT* is heated. Two-phase flow with increasing temperature will reach the top region of the circular closed tube. Two-phase fluid will condense because of lower temperature therein as the heated liquid will become vapor and then condense into liquid and back into the evaporation zone.

Table 1
The boundary conditions.

Regions	Momentum	Thermal
Heating	No Inlets & Outlets	Convection (T = 355 K; $\overline{h}_{water,L_{heating}}$ from Eq.7)
Cooling	No Inlets & Outlets	Convection (T = 300 K; $\overline{h}_{air,L_{cooling}}$ from Eq.9)

2.2. Numerical modelling

In this study, the thermal performance of the copper *TPCT* was numerically investigated to obtain the numerical distribution of temperature and steam volume fraction by using *VOF* and Eulerian multiphase models. For this, the general approach to the modeling of *TPCT* requires the development of mathematical formulations. A mathematical model obtained from thermodynamic laws and suitable assumptions has been used for numerical thermal performance analysis. Governing equations using in the mathematical model are the conservation of mass, momentum, and energy. The solution of these equations is to be obtained simultaneously.

VOF and Eulerian models are selected as the multiphase model for new combined numerical analysis. *VOF* model is designed to track the location and motion of free surface between two or more immiscible fluids. Eulerian multiphase model is the multi-fluid model, and the conservation equations for each phase contain single-phase terms (pressure-gradient, thermal conduction, etc.) and interfacial terms (drag, lift, mass transfer, etc.) [19]. In each control volume, volume fractions of all phases sum to unity. a and b to represent fluids: If the a^{th} fluid's volume fraction in cell is denoted as α_b, then the following three conditions are possible:

- $\alpha_b = 0$: The cell is empty (of the b^{th} fluid).
- $\alpha_b = 1$: The cell is full (of the b^{th} fluid).
- $0 < \alpha_b < 1$: The cell contains the interface between the b^{th} fluid and one or more other fluids.

The tracking of interfaces between the phases is accomplished by the solution of the mass conservation equation for the volume fraction of phases. For the b^{th} phase, this equation has the following form [21]:

$$\frac{1}{\rho_b}\left[\frac{\partial}{\partial t}(\alpha_b\rho_b) + \nabla.\left(\alpha_b\rho_b\overrightarrow{V}_b\right) = S_m + \sum_{p=1}^{n}\left(\dot{m}_{ab} - \dot{m}_{ba}\right)\right] \quad (1)$$

here $\dot{m}_{ba}$ is the mass transfer from phase b to phase a and $\dot{m}_{ab}$ is the mass transfer from phase a to phase b and S_m is mass source term. The momentum equation is dependent on the volume fractions of all phases through the properties ρ and μ for *VOF* [32]:

$$\frac{\partial}{\partial t}\left(\rho\overrightarrow{V}\right) + \nabla.\left(\rho\overrightarrow{V}\overrightarrow{V}\right) = -\nabla p + \rho\overrightarrow{g} + \nabla.\left[\mu\left(\nabla\overrightarrow{V} + \nabla\overrightarrow{V}^{T}\right)\right] + \overrightarrow{F}_{st} \quad (2)$$

here P is pressure, μ is dynamic viscosity, $\overrightarrow{g}$ is the acceleration of gravity, and $\overrightarrow{F}_{st}$ is surface tension force. The force at the surface can be expressed as a volume force using the divergence theorem for two phases in a cell [33,34]. Energy equation, also shared among phases, is shown below [31]:

$$\frac{\partial}{\partial t}(\rho E) + \nabla.\left(\overrightarrow{V}(\rho E + p)\right) = \nabla.(k\nabla T) + S_E \quad (3)$$

here T is temperature, S_E denotes energy source term, and E for each phase is based on the specific heat of that phase and shared temperature, k is thermal conductivity:

$$k = \alpha_a k_a + (1 - \alpha_a)k_b \quad (4)$$

The source term for the energy equation can be obtained by multiplying the rate of mass transfer by the latent heat. These equations are discretized using a control volume approach by iterative means of complex equations, which can be easily solved by using *CFD* software numerically.

As can be seen in Fig. 1, the first 100 mm long section from the bottom of the *TPCT* is immersed in the heated water at the temperature of 355 K while the surfaces of the rest of the *TPCT* are in contact with the air at the temperature of 300 K in an open environment to the atmosphere. For this reason, the total heat transfer coefficients for the heated water and ambient air must be found to describe as the boundary conditions in *CFD* modeling. These coefficients can be calculated by using the empirical formulations from the literature. Moreover, a detailed experimental analysis has been performed to assist the empirical formulations providing the surface temperatures to depend on time. Besides, Nusselt and Rayleigh numbers depending on the natural convection can be calculated to utilize the heat transfer coefficient correlations. For this reason, the Nusselt and Rayleigh numbers for the outer surfaces of the *TPCT* with the length of L and diameter of D is given [35,36]:

$$\overline{Nu}_L = \frac{4}{3}\left[\frac{7Ra_L Pr}{5(20 + 21Pr)}\right]^{1/4} + \frac{4(272 + 315Pr)L}{35(64 + 63Pr)D} \quad (5)$$

$$Ra_L = \frac{g\beta\Delta TL^3}{\alpha\nu} \quad (6)$$

here $\Delta T$is the temperature difference between the pipe surface and the fluid reservoir while α denotes the thermal diffusivity. Eqs. (5) and (6) are utilized to calculate the heat transfer coefficient of water and air in the following equations of (7) and (9). Although Eq. (5) is valid for all Rayleigh numbers, this equation is only used for the circumstance of $D/L > Ra_L^{-1/4}$. The wall-averaged heat transfer coefficient and the total heat transfer rate of water around the length of the heating region ($L_{heating}$) of the *TPCT* are calculated as:

$$\overline{h}_{water,L_{heating}} = \frac{k.\overline{Nu}_{L_{heating}}}{L_{heating}} \quad (7)$$

$$\dot{Q}_{heating} = \overline{h}_{water,L_{heating}}\left(\pi \times D \times L_{heating}\right)\left(T_{heat} - T_{s,heating}\right) \quad (8)$$

here $\dot{Q}_{heating}$, T_{heat} and $T_{s,heating}$ are the heat transferred to the heating region from the heat source, the temperatures of the heat source, and the heating surface, respectively. Also, the wall-averaged heat transfer coefficient and the total heat transfer rate of air around the cooling region ($L_{cooling}$) of the *TPCT* are calculated as:

$$\overline{h}_{air,L_{cooling}} = \frac{k.\overline{Nu}_{L_{cooling}}}{L_{cooling}} \quad (9)$$

$$\dot{Q}_{cooling} = \overline{h}_{air,L_{cooling}}\left(\pi \times D \times L_{cooling}\right)\left(T_{s,cooling} - T_{amb}\right) \quad (10)$$

here $\dot{Q}_{cooling}$, T_{amb} and $T_{s,cooling}$ are the heat transferred to ambient from cooling region, the temperatures of ambient and condensation surface, respectively. In order to perform numerical analysis, the geometry of *TPCT* is designed, and the named selections of that are defined by using ANSYS 15.0 software. The geometry of *TPCT* is formed employing Design Modeler in Fluent. The lengths of heating and cooling regions are 100 mm and 1400 mm, respectively. Also, the first 25 mm of the heating is filled with water liquid of 10 ml while the other length of 1475 mm of the *TPCT* inside is filled the air at a low density. The boundary conditions of this numerical study are given in Table 1.

According to Table 1, there are no inlets and outlets for the momentum boundary condition; the system is considered as the closed pipe. Besides, thermal boundary conditions are defined as the convection of heated water at the temperature of 355 K and ambient air at the temperature of 300 K. $\overline{h}_{water,L_{heating}}$ and $\overline{h}_{air,L_{cooling}}$ values are calculated with the detailed time-depended experimental data from Eq.7 and Eq.9, respectively. Besides, Coupled option was selected with the solid material for the inside wall interface because the solver calculated the heat

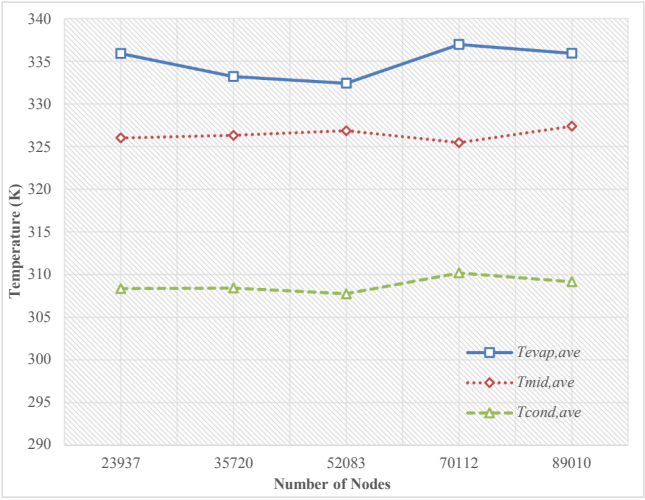

Fig. 2. The change of average temperatures in different regions for five different mesh numbers of nodes.

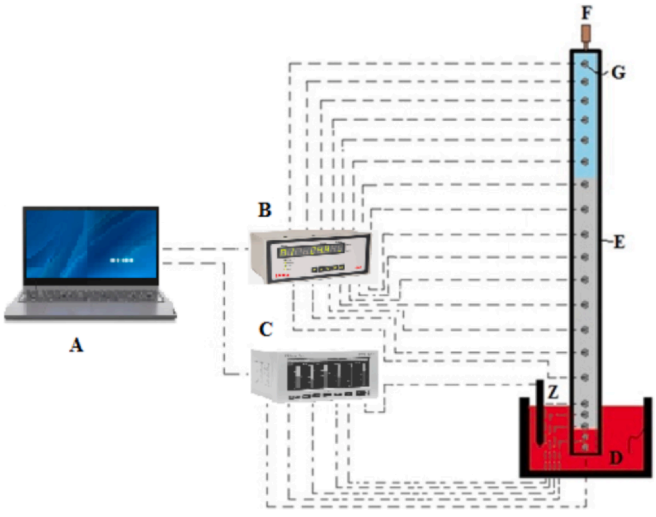

Fig. 3. The flow diagram of the designed test apparatus.

transfer directly from the solution in the adjacent cells. On the other hand, the heat power of 100 W, 150 W, 200 W, and 250 W is applied in the heating region while the convection heat transfer coefficient of ambient air is calculated by using Eq. (9) with the ambient temperature of 300 K in the cooling part for the parametrical study.

VOF model was selected as the first multiphase model with the evaporation–condensation mechanism that uses the improved Lee model by changing the evaporation and condensation coefficients. The Eulerian model was selected as the second multiphase model with the Eulerian parameter of evaporation–condensation model with the improved Lee model. The continuum surface force with wall adhesion option was also utilized in the surface tension force modeling in both *VOF* and Eulerian multiphase models. For the evaporation–condensation mechanism, the average saturation temperature is constant as 309.93 K at 6 kPa for *VOF* and 330.15 K at 17.5 kPa for Eulerian multiphase model [37,38]. The steam density of 0.0787 kg/m^3 in the *VOF* model and the 0.1153 kg/m^3 in the Eulerian model are selected as the average values according to the pressure inside the *TPCT*. The air density in *VOF* model is calculated as the space in the pipe at the beginning of vacuumed pressure. On the other hand, the values of water density (ρ_{water}) and surface tension (σ_{w-s}) between phases for two multiphase are calculated by using the following equations:

$$\rho_{water} = 750.4359 + 2.14358 \times T - 0.0051 \times T^2 + 2.27243e^{-06} \times T^3 \quad (11)$$

$$\sigma_{w-s} = 0.083112 + 0.000107 \times T - 5.8e^{-07} \times T^2 + 3.15661e^{-10} \times T^3 \quad (12)$$

These correlations (Eqs. (11) and (12)) were defined in Materials and Setting Up Physics in Setup of Fluent. By this means, ρ_{water} and σ_{w-s} values have been calculated for different temperature values inside copper and glass *TPCTs* for Eulerian multiphase model. Moreover, the fluids' physical properties are assumed that constant as the averaged values according to the experimental results. Moreover, copper and glass solid physical properties were defined in Materials and Setting Up Physics in Setup of Fluent. Also, all physical properties of air, water liquid, and water vapor were obtained from REFPROP 9.0 database [39]. The way performed for meshing is Cutcell mesh method. The generating mesh has 52,089 nodes and 47,168 elements. Average orthogonal quality and skewness are 0.979 and 0.077, respectively. Mesh independence study is given in Fig. 2 as the change of average temperatures (a) in the three different regions in the *TPCT* for five different mesh number of nodes.

As shown in Fig. 2, the differences in the change of average temperatures in three different regions are reasonable for five different mesh numbers of nodes. Because of this, mesh independence is ensured for this numerical study. Thermal resistance (R) of *TPCT* is defined [40,41]:

$$R = \frac{\left(T_{evap,ave} - T_{cond,ave}\right)}{\dot{Q}_{heating}} \quad (13)$$

k–ε turbulence model, which is used in the most general multiphase turbulence, was applied in both *VOF* and *Eulerian* multiphase models. Nevertheless, different turbulence models like *LES*, *k-kl* ω transition, *k-ω*, *SAS*, and *Re-Stress* with k–ε were examined in *VOF* which have more turbulence options than Eulerian for comparing them. There are different turbulence models in *CFD* to use simulating the *TPCT*. The standard k- ε model contains transport equations for turbulence kinetic energy(k) and its dissipation rate(ε). The transport equation for k is derived from the exact equation while the transport equation for ε has been acquired using physical reasoning. Realizable k–ε model, ε-equation is derived from the mean-square vorticity fluctuation, which is fundamentally different from the standard k–ε model.

On the other hand, standard *k-ω* composing k and its specific dissipation rate include the modifications for low-Reynolds number effects, compressibility, and shear flow distribution. Shear-stress transport (*SST*) *k-ω* model has used to blend the strong and explicit formulation of *k-ω* model in the near-wall region with freestream independence of *k-ε* model in the far-field. Reynolds Stress Model (*RSM*) that closes Reynolds-averaged Navier-Stokes (*RANS*) equations solve the transport equations for Reynolds stresses, together with an equation for dissipation rate. Besides, the *k-kl* ω transition model that can be used to effectively address the transition of the boundary layer from laminar to turbulent regime is used to predict boundary layer development and calculate transition onset. In Large Eddy Simulation (*LES*), are resolved directly, while small eddies are modeled. *LES* that mostly transports momentum, mass, energy, and other passive scalars fall between direct numerical simulation and *RANS* in terms of the fraction of resolved scales. Scale-Adaptive Simulation (*SAS*) modeling is an approach for the simulation of unsteady turbulent flows and can be applied in combination with most ω-based unsteady *RANS* (*URANS*) turbulence models. *SAS* can be selected in order to apply it in combination with the *SST k-ω* turbulence model [42–45].

The new combined numerical analysis of *TPCTs* has been performed as the unsteady-state regime. For this purpose, *VOF* model has been used for the first 60 s, and Eulerian model has been employed after 60 s until 180 s because the temperature distribution inside *TPCT* becomes uniform until 60 s, and then it changes a little [21]. The numerical analysis was performed by using *VOF* model for the first 60 s. After completed the numerical analysis used *VOF* model, the numerical study used Eulerian

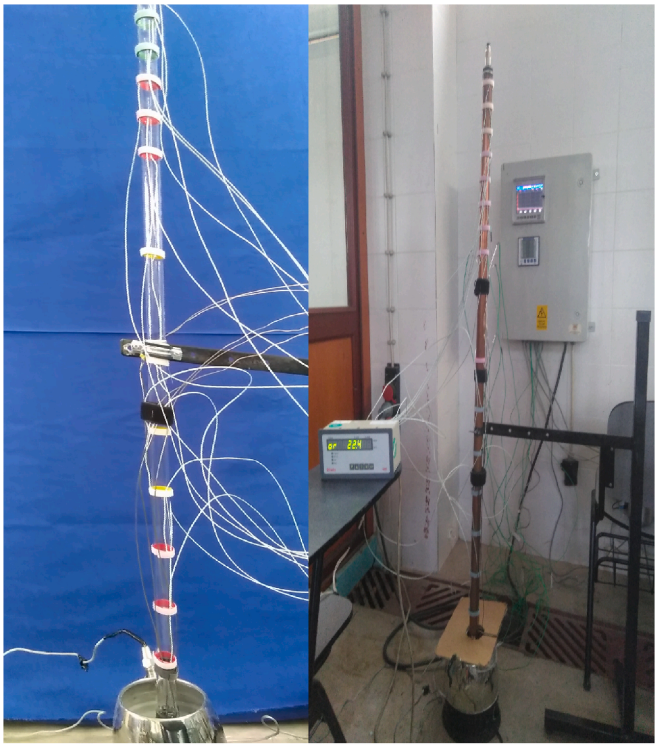

Fig. 4. The test apparatus and the ambient of that. (a) glass pipe, (b) copper pipe.

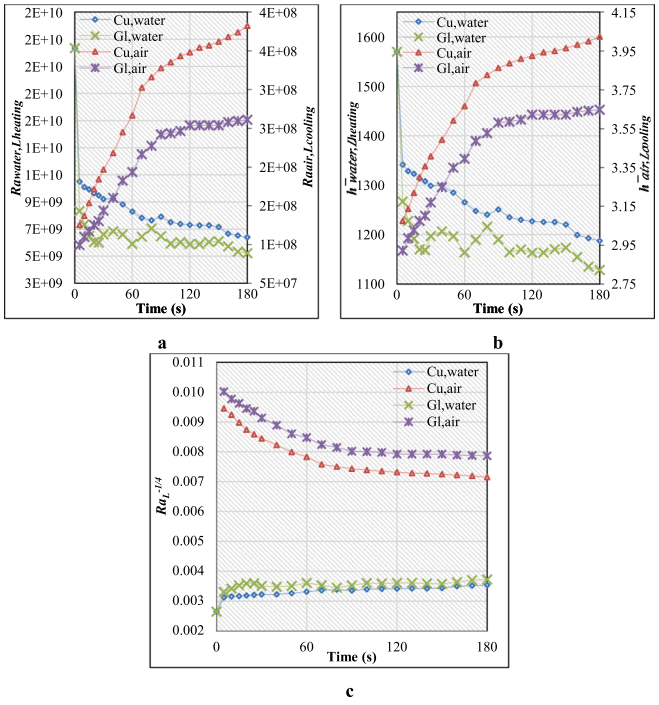

Fig. 5. The change of experimental (a) $Ra_{water.L_{heating}}$, $Ra_{air.L_{cooling}}$, (b) $\overline{h}_{water.L_{heating}}$, $\overline{h}_{air.L_{cooling}}$, and (c) $Ra_L^{-1/4}$ values for water and air in the glass and copper *TPCTs*.

model was performed by using the other boundary conditions. Besides, the numerical computation is considered to have converged when the scaled residual of the mass and velocity components is less than 10^{-4}. The simulation was done on a 64-bit Windows 10 Dell workstation with a 2.20 GHz Intel® Xeon® CPU E5-2630 v4 and 32 GB RAM.

On the other hand, the experimental analysis in detail was performed to define exact boundary conditions and verify the numerical model.

Table 2
Solution methods for *VOF* and Eulerian models.

Methods	*VOF* Model	Eulerian model
Scheme	SIMPLE	Phase Coupled SIMPLE
Gradient	Least Squares Cell-Based	Least Squares Cell-Based
Momentum	Second-Order Upwind	Second-Order Upwind
Volume Fraction	Geo-Reconstruct	Modified HRIC
Turbulent Kinetic Energy	Second-Order Upwind	Second-Order Upwind
Turbulent Dissipation Rate	Second-Order Upwind	Second-Order Upwind
Energy	Second-Order Upwind	Second-Order Upwind
Transient Formulation	Second-Order Implicit	Second-Order Implicit

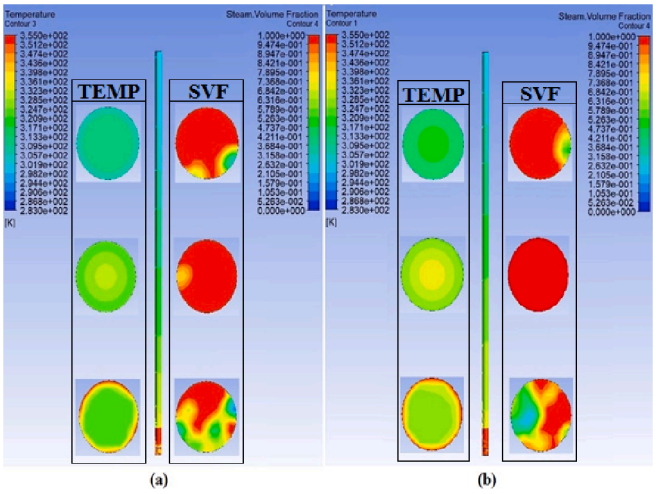

Fig. 6. 3D temperature distribution (TEMP) and the steam volume fraction (SVF) contour profiles of the different regions of (a) glass and (b) copper *TPCT* at the end of the numerical study of *VOF* model.

2.3. Experimental modelling

The verification of the numerical thermal analysis of the *TPCT* is provided by the experimental study design [46]. According to this, the accuracy of the model obtained by the CFD study can be tested. The flow diagram of the designed test apparatus is given in Fig. 3.

According to Fig. 3, the designed test apparatus consists of a computer (A), data loggers (B-C), a heat source (D), *TPCT* (E), manometer (F), thermocouples (G-Z). The *TPCT* material is chosen as glass and copper; the inner, outer diameter, and length of the *TPCT* are selected as 26 mm, 28 mm, and 1500 mm, respectively. Also, the vacuum pressure of the copper pipe inside is 6 kPa. This pipe is dipped in the heat source that has the water at a constant temperature of 355 K. The temperature distribution of the *TPCT* was measured using twenty different positions, as shown in Fig. 4. Both glass and copper pipes were filled the water volume of 10 ml. Also, thermal and video camera images were recorded for the glass *TPCT* to view the physical situations.

According to the experimental setup, the seven different thermocouples were used to record the average temperature of the evaporation region, while the eight different thermocouples were used to record the average temperature of the condensation region [38]. Besides, the five different thermocouples were used to record the average temperature of the evaporation region.

The average temperature of the evaporation ($T_{evap,ave}$), middle ($T_{mid,ave}$), and condensation ($T_{cond,ave}$) for different regions were monitored both numerically and experimentally. The measurements were evaluated with the uncertainty analysis. The average of the measured

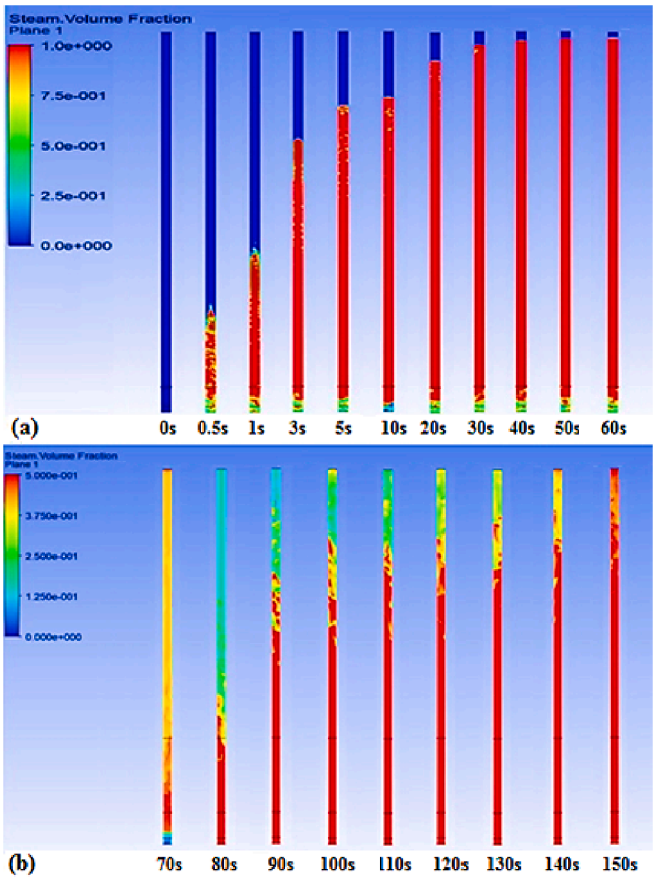

Fig. 7. The numerical steam volume fraction change of glass *TPCT* in *VOF* and Eulerian models.

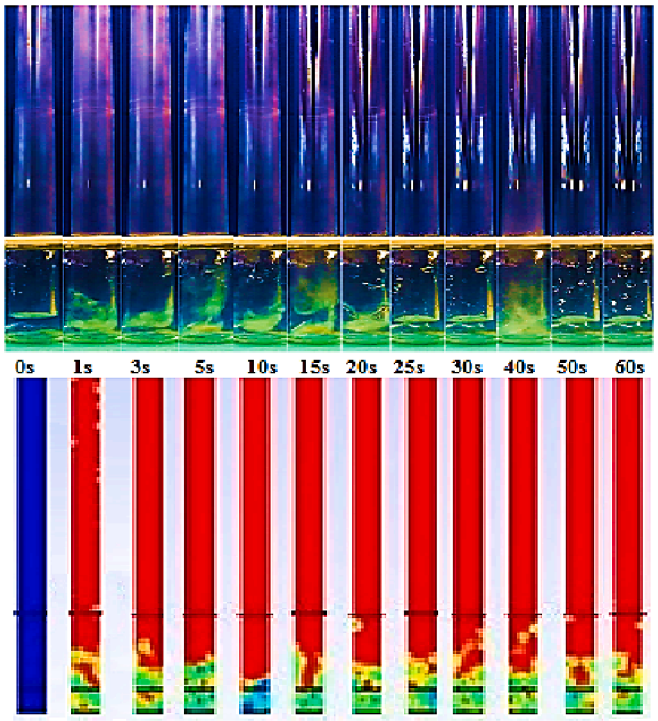

Fig. 8. The comparison of *EXP* and *CFD* steam volumes in evaporation region of glass *TPCT*.

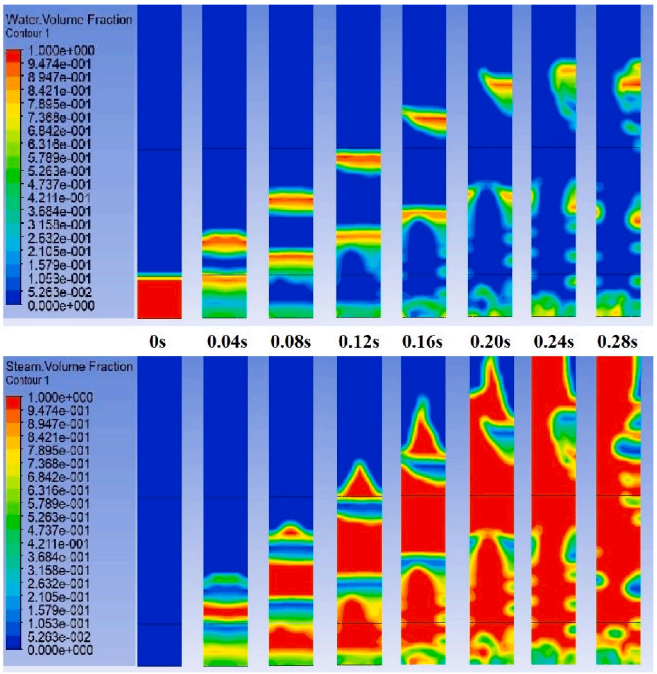

Fig. 9. The change of water and steam volume fractions in the evaporation region of glass *TPCT* for the early beginning of the numerical analysis.

values is given by:

$$\overline{X} = \frac{\sum X_m}{n} \tag{14}$$

Where n; the numbers of the measurement and X_m; the measured value. Standard deviation is given as follows:

$$SD = \sqrt{\frac{\sum_{m=1}^{n}(X_m - \overline{X})^2}{(n-1)}} \tag{15}$$

Then, uncertainty is given as following [47];

$$U = \frac{SD}{\sqrt{n}} \tag{16}$$

2.4. Comparison of numerical and experimental modeling

It is necessary to compare the numerical and experimental models to indicate how close the numerical model created is. Therefore, the numerical and experimental results have been compared with each other by using the absolute temperature difference, which is calculated as:

$$\Delta T_{abs} = |T_{EXP} - T_{CFD}| \tag{17}$$

where T_{EXP} and T_{CFD} denote the experimental and numerical temperature at any situation to be compared, respectively. Beside this, the obtained values from the numerical modelling can be assessed in point of statistical. For this purpose, the performance of some thermocouples in a numerical model is determined by using statistical methods like the error of the square root (*RMSE*), the coefficient of variation (*cov*), the percentage of absolute change (R^2), and the mean percentage error (*MPE*) as given in the following equalities:

$$RMSE = \sqrt{\frac{\sum_{m=1}^{n}\left(\frac{y_{output} - y_{actual}}{y_{output}}\right)^2}{n}} \tag{18}$$

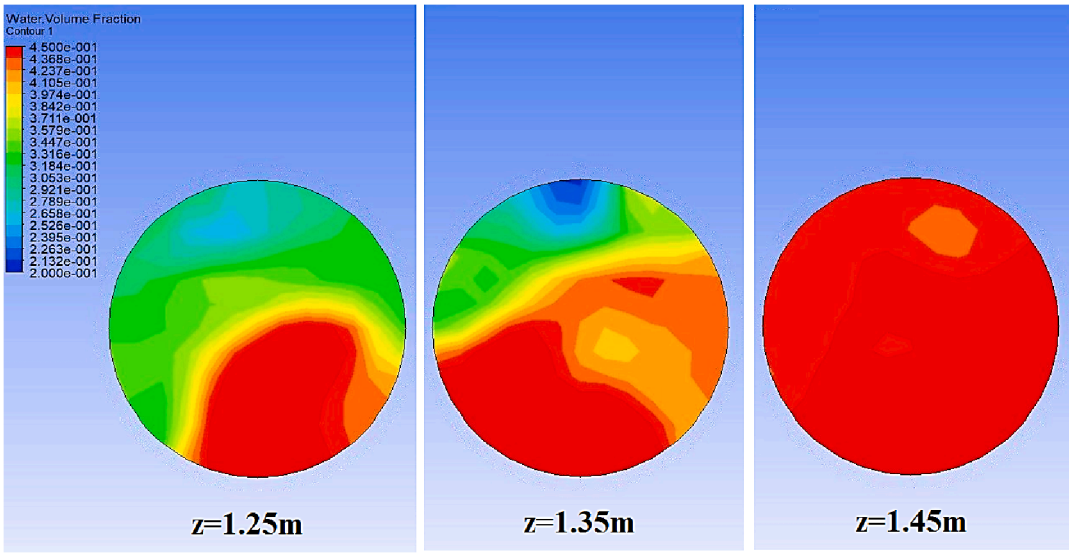

Fig. 10. change of water volume fractions in the condensation region of glass *TPCT* for different height values at the end of the numerical analysis.

$$cov = \frac{\sum_{m=1}^{n}\left(y_{output}-\overline{y}_{output}\right)\left(y_{actual}-\overline{y}_{actual}\right)}{n}\text{x}100 \tag{19}$$

$$R^2 = \left[\frac{\sum_{m=1}^{n}\left(y_{output}-\overline{y}_{output}\right)\left(y_{actual}-\overline{y}_{actual}\right)}{\sqrt{\sum_{m=1}^{n}\left(y_{output}-\overline{y}_{output}\right)^2\sum_{m=1}^{n}\left(y_{actual}-\overline{y}_{actual}\right)^2}}\right]^2 \tag{20}$$

$$MPE = \frac{\sum_{m=1}^{n}\left(y_{output}-y_{actual}\right)}{n\times\left|y_{actual,max}-y_{actual,min}\right|}\times 100 \tag{21}$$

Here, y_{output}; is the output value, $\overline{y}_{output}$; is the average output value, y_{actual}; is the actual value, $\overline{y}_{actual}$; is the average actual value, and n is the number of values [48,49].

3. Results and discussion

A comprehensive experimental and numerical study was performed for the thermal performance analysis of the glass and copper *TPCTs* in detail. The calculated $\overline{h}_{water,L_{heating}}$ with the temperature of 355 K and $\overline{h}_{air,L_{cooling}}$ with the temperature of 300 K values were used for the boundary conditions of the heating and cooling regions, respectively. The change of experimental Rayleigh, $\overline{h}_{water,L_{heating}}$, $\overline{h}_{air,L_{cooling}}$, and $Ra_L^{-1/4}$ values for water and air in the glass and copper *TPCTs* were given in Fig. 5.

According to Fig. 5a, $Ra_{water,L_{heating}}$ values have decreased with increasing time while $Ra_{air,L_{cooling}}$ values have increased. $Ra_{water,L_{heating}}$ values have changed between 2.03×10^{10} and 5.21×10^{9} while $Ra_{air,L_{cooling}}$ values were the range of 9.94×10^{7}–3.82×10^{8}. According to Fig. 5b, $\overline{h}_{water,L_{heating}}$ values showed a similar trend with $Ra_{water,L_{heating}}$ values while $\overline{h}_{air,L_{cooling}}$ values demonstrated similar propensity with $Ra_{air,L_{cooling}}$ for copper and glass pipes.$\overline{h}_{air,L_{cooling}}$ values for copper and glass pipes have changed a little after 90th second, and the average $\overline{h}_{air,L_{cooling}}$ values for copper and glass pipes were calculated as 3.945 W/m^{2}K and 3.618 W/m^{2}K after that time. Besides, the maximum $\overline{h}_{water,L_{heating}}$ values for copper and glass pipes were calculated as 1569.91 W/m^{2}K at the beginning of the experiments. These coefficients obtained from Fig. 5b were applied as the average values for *VOF* (first 60 s) and Eulerian (60–180 s) boundary conditions. For the convection boundary conditions in *VOF* model, the average $\overline{h}_{water,L_{heating}}$ values were calculated as 1307.08 W/m^{2}K and 1198.74 W/m^{2}K while average $\overline{h}_{air,L_{cooling}}$ values were 3.36 W/m^{2}K and 3.14 W/m^{2}K for copper and glass pipes, respectively. On the other hand, for the convection boundary conditions in Eulerian model, the average $\overline{h}_{water,L_{heating}}$ values were calculated as 1223.43 W/m^{2}K and 1168.21 W/m^{2}K, while average $\overline{h}_{air,L_{cooling}}$ values were 3.92 W/m^{2}K and 3.60 W/m^{2}K for copper and glass pipes, respectively. According to Fig. 5c, the maximum $Ra_L^{-1/4}$ values for copper and glass pipes were calculated as 0.0035 and 0.0037 in the convection of water at the heating region. These values were 0.0095 and 0.0101 in the convection of air at the cooling region, respectively. On the other hand, the calculated $\overline{h}_{water,L_{heating}}$ and $\overline{h}_{air,L_{cooling}}$ values were defined as valid because D/L values were calculated as 0.28 and 0.0467 for the heating and cooling regions, respectively.

A new combined numerical model of the *TPCT* was composed of *3D* and analyzed thermodynamically using ANSYS Fluent 15 software. Solution methods for this new model composed of two stages that were *VOF* and Eulerian multiphase models are defined as Table 2.

The methods for *VOF* and Eulerian models in Table 2 were used, and hybrid initializing was done. After initializing, the regions that later be filled with one of the phases were marked. This provides a quick approximation of the flow field by a collection of methods.

3.1. Experimental and numerical results of TPCTs

The numerical analysis results can be attained in many manners such as contours, streamlines, graphs, etc. The three-dimensional (*3D*) temperature distribution (TEMP) and the steam volume fraction (SVF) contour profiles of all external surfaces and cross-sections at different lengths (45 mm, 450 mm, and 1100 mm) of glass and copper *TPCTs* at the end of the numerical study of *VOF* model are shown in Fig. 6.

According to Fig. 6, it was observed that the surface temperature values of the glass (6a) and copper *TPCT* (6b) ranged between 293 K and 355 K, and these values have decreased from the evaporation region to the condensation region. The change of temperature has been shown as the contour profiles, which make clear the distribution of that. The left side has shown the temperature distribution while the right side demonstrates the change of the steam volume fraction at three different lengths (45 mm, 450 mm, and 1100 mm) of the glass and copper *TPCTs*. On the other hand, there was no air except for the little top section of the *TPCT* at the end of the analysis. Therefore, the change of the air volume

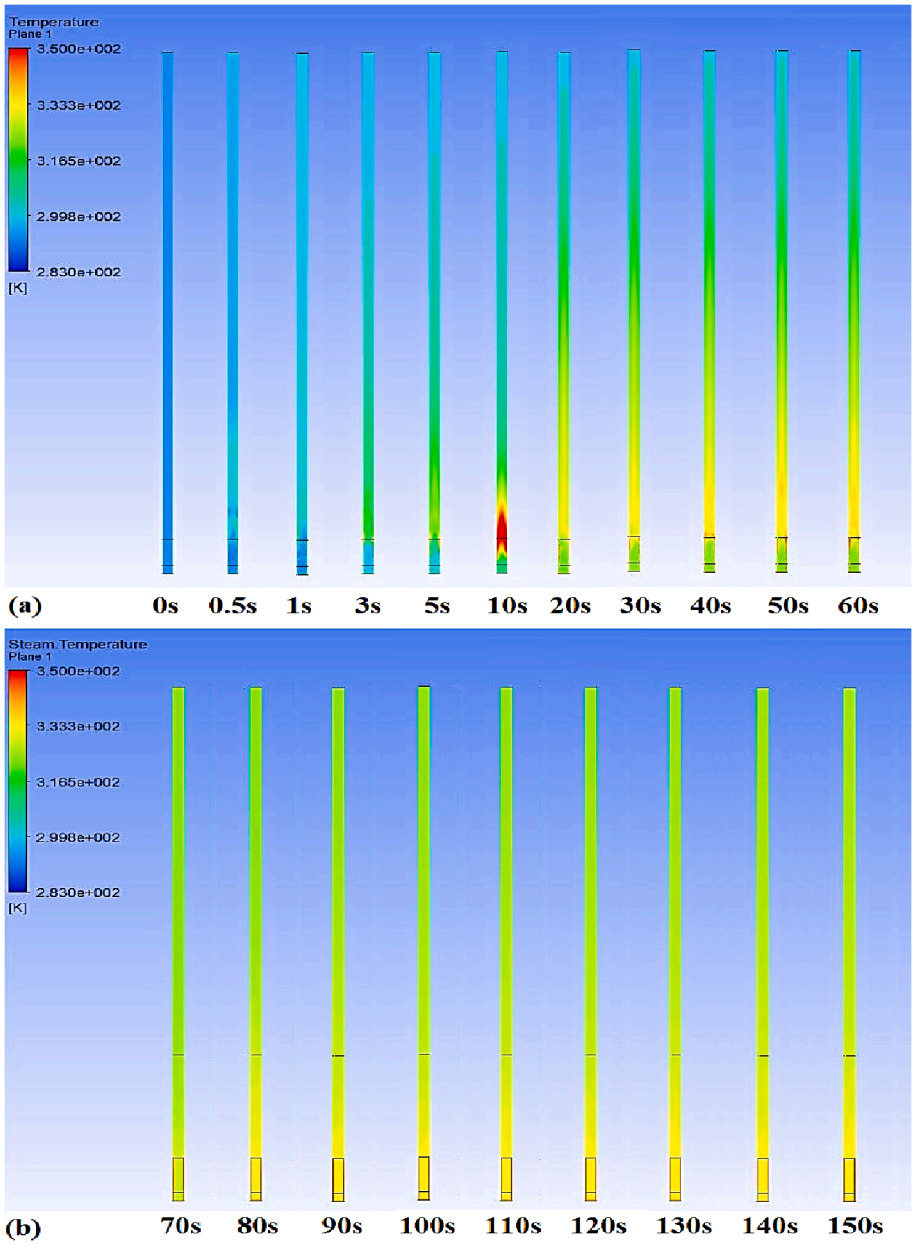

Fig. 11. The numerical temperature change of glass *TPCT* in *VOF* and Eulerian models.

fraction has not been shown in Fig. 6. The numerical steam volume fraction change of glass *TPCT* in *VOF* and Eulerian models is given in Fig. 7.

According to Fig. 7a, the numerical steam volume change in glass *TPCT* has changed between 0 and 1. The steam volume of glass *TPCT* is zero at the beginning of the analysis. After starting the analysis, the water at the glass pipe's evaporation region starts to boil and evaporate through the middle region at the other time steps. The steam reaches the condensation region after 3 s and it takes up nearly all condensation regions after 40 s. The process of evaporating and condensing concurs along the *TPCT* in all regions. According to Fig. 7b, it is seen that the numerical steam volume in glass *TPCT* obtained by using the *VOF* model for the first 60 s have increased from 70th second to 140th second using the Eulerian model, after which it did not change so much until the end of the numerical analysis. It was observed that the steam volume has rapidly increased at the beginning, and then it has slightly decreased with condensation, and there was a stable change in the range of 100 s-130 s. The comparison of experimental (*EXP*) and numerical (*CFD*) steam volumes in the evaporation region of glass *TPCT* is given in Fig. 8.

According to Fig. 8 there is no occurred a long duration sub-cooled boiling and bubbly flow like the literature because *TPCT* is vacuumed until the pressure of 6.32 kPa (the saturation temperature of 309.78 K). Moreover, the slug flow has suddenly occurred as *TPCT* is immersed in a heat source with 355 K which is more higher than 309.78 K. Besides, the geyser boiling occurred with pulsating at some times as shown in experimental steam volume change clearly. The change of water and steam volume fractions in the evaporation region of glass *TPCT* for the early beginning of the numerical analysis is given in Fig. 9.

According to Fig. 9, the water volume fractions were accordance with the steam volume fractions between 0 s and 0.28 s. There was no certain bubbly flow because *TPCT* was suddenly immersed in a heat source with a temperature well above the saturation temperature at under atmosphere pressure. The formation vapor slugs have become clear after 0.12 s, and the annular flow began to be in sight. After 0.20 s, the steam particles exploded and started to condense, and this process have repeated with continuing the boiling. These steam volume

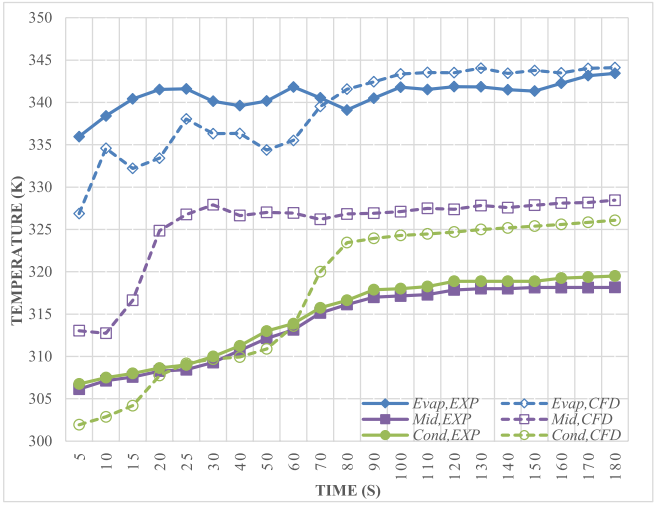

Fig.12. $T_{evap,ave}$, $T_{mid,ave}$, and $T_{cond,ave}$ values between experimental results and numerical analysis for glass *TPCT* for different time steps.

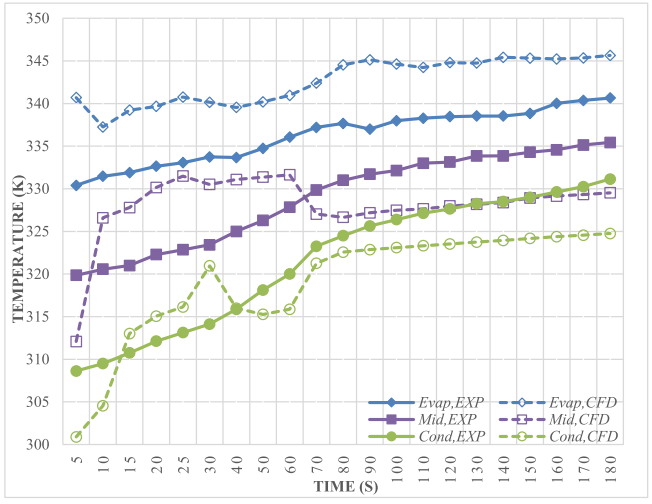

Fig.13. $T_{evap,ave}$, $T_{mid,ave}$, and $T_{cond,ave}$ values between experimental results and numerical analysis for copper *TPCT* for different time steps.

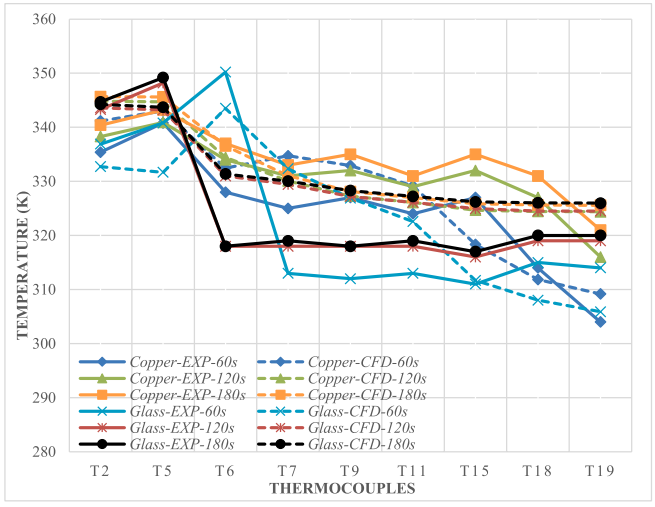

Fig.14. The change of *EXP* and *CFD* temperatures in some thermocouples in copper and glass *TPCTs* for 60 s, 120 s, and 180 s.

formations were obtained as similar to bubble growth behaviors from Wang et al.'s study in the literature [30]. Also, Wang et al. have used the improved Lee model and the saturation temperature at vacuum pressure not atmosphere pressure (T_{sat} = 373 K) like in this study. The change of water volume fractions in the condensation region of glass *TPCT* for different height values at the end of the numerical analysis is given in Fig. 10.

According to Fig. 10, the water volume fraction values have increased as the height value of glass *TPCT* was raised from 1.25 m to 1.45 m. It was clear that the water and steam volumes were nested in the cross-section of *TPCT*. The numerical temperature change of glass *TPCT* in *VOF* and Eulerian models is given in Fig. 11.

According to Fig. 11a, the numerical temperature of glass *TPCT* has increased with the time steps and the values of that have changed between 293 K and 355 K. While the temperature of the evaporation region reaches 355 K at the time of 10 s, the temperature of the other regions of *TPCT* have nearly increased after this time. On the other hand, the temperature distribution of every region has not changed so much from 30 s to 60 s. According to Fig. 11b, while the average temperature of the evaporation region in the 70th seconds is 339.52 K, this value reaches 344.11 K at the end of the analysis. On the other hand, the average temperature values of the middle and condensation regions have increased from 326.19 K and 320.02 K to 328.45 K and 326.08 K, respectively. From the 70th seconds to the end of the numerical analysis, it is seen that the temperature has not changed so much but increased slightly.

The results of the numerical and experimental need to conform with each other to validate the numerical model. $T_{evap,ave}$, $T_{mid,ave}$, and $T_{cond,ave}$ values between experimental results and numerical analysis for glass *TPCT* for different time steps were given in Fig. 12.

According to Fig. 12, the numerical $T_{evap,ave}$ and $T_{cond,ave}$ values of glass *TPCT* showed a similar trend as the experimental of that while the numerical $T_{mid,ave}$, values have more deviation than the others. On the other hand, the experimental $T_{mid,ave}$ and $T_{cond,ave}$ values were close to each other while the numerical $T_{mid,ave}$ and $T_{cond,ave}$ values have shown a close trend after 80th second. The maximum ΔT_{abs} values were obtained as 9.09 K at 5th second, 18.63 K at 30th second, and 6.81 K at 80th second in the evaporation, middle, and condensation regions, respectively. $T_{evap,ave}$, $T_{mid,ave}$, and $T_{cond,ave}$ values between experimental results and numerical analysis for copper *TPCT* for different time steps were given in Fig. 13.

According to Fig. 13, $T_{evap,ave}$, $T_{mid,ave}$, and $T_{cond,ave}$ values between experimental results and numerical analysis have shown similar trend with some deviations to each other for copper *TPCT* for different time steps. Besides, the numerical and experimental of $T_{mid,ave}$ and $T_{cond,ave}$ values have shown a similar trend with fluctuations for different time steps.

The maximumΔT_{abs} values were obtained as 10.30 K at 5th second, 8.64 K at 25th second, and 7.74 K at 5th second in the evaporation, middle, and condensation regions, respectively. The change of *EXP* and *CFD* temperatures in some thermocouples in copper and glass *TPCTs* for 60 s, 120 s, and 180 s was given in Fig. 14.

According to Fig. 14, while the maximum deviation between temperature values occurred in the T7 at 60th second in the glass *TPCT*, the minimum deviation occurred in T6 at the 120th second in the copper *TPCT*. The maximum ΔT_{abs} values were obtained as 9.73 K in T7, 8.37 K in T19, and 9.14 K in T15 at 60, 120, and 180 s, respectively, for the copper *TPCT*. On the other hand, the maximum ΔT_{abs} values were obtained as 19.34 K in T7, 13 K in T6, and 13.36 K in T6 at 60, 120, and 180 s, respectively for the glass *TPCT*. The thermocouples' statistical results in Fig. 14 in copper and glass *TPCTs* for 60 s, 120 s, and 180 s were given in Table 3.

According to Table 3, the statistical values belonging to 60th second for copper *TPCT* showed the best result (R^2 = 0.93) while the statistical values belonging to 60th second for glass *TPCT* demonstrated the worst

Table 3
The thermocouples' statistical results in Fig. 14 in copper and glass *TPCTs* for 60 s, 120 s, and 180 s.

Time (s)	*cov*		*MPE*		*RMSE*		R^2	
	Copper	Glass	Copper	Glass	Copper	Glass	Copper	Glass
60	1.61	3.18	12.24	22.56	5.22	10.26	0.93	0.51
120	1.29	2.55	13.49	24.17	4.29	8.27	0.69	0.89
180	1.23	2.64	15.46	24.17	4.09	8.57	0.71	0.91

Table 4
Technical properties of the measurement devices.

Measurement Devices	Technical Properties	Accuracy
Thermocouples (T1 - T20)	K-type thermocouple.	±1.5 °C or ± 1.5% of measurement value (Whichever is greater)
Vacuum Manometer	Pakkens, Analog Ø100 Manometer.	±1% over full scale.
Data Logger-1	Elimko PR-100, 12 channels.	±0.5% of recording value or ± 1 °C.
Data Logger-2	Elimko E-680 32 channels.	±0.5% of recording value.

Table 5
The average of the measured values, standard deviation, and the measurement equipment's uncertainty for copper and glass *TPCTs*.

Measurement Equipment	Glass Pipe			Copper Pipe		
	$\overline{X}$	*SD*	*U*	$\overline{X}$	*SD*	*U*
T1	60.88	4.94	±0.32 K	64.50	6.54	±0.27 K
T2	64.15	7.33	±0.48 K	65.61	6.08	±0.25 K
T3	63.66	4.99	±0.33 K	63.21	7.23	±0.30 K
T4	61.74	7.88	±0.52 K	65.30	6.88	±0.29 K
T5	75.99	4.81	±0.32 K	67.35	6.12	±0.25 K
T6	36.68	7.98	±0.52 K	60.23	10.03	±0.42 K
T7	36.43	8.17	±0.54 K	56.88	9.75	±0.40 K
T8	36.77	7.83	±0.51 K	63.51	9.57	±0.39 K
T9	37.58	7.77	±0.51 K	58.19	9.72	±0.40 K
T10	36.46	7.05	±0.46 K	59.99	10.41	±0.43 K
T11	37.51	7.67	±0.50 K	54.71	9.66	±0.40 K
T12	36.57	7.79	±0.51 K	58.83	10.54	±0.44 K
T13	36.51	7.86	±0.52 K	61.91	11.62	±0.48 K
T14	38.21	8.41	±0.55 K	61.09	11.99	±0.50 K
T15	35.48	7.08	±0.46 K	56.86	11.75	±0.49 K
T16	37.50	8.21	±0.54 K	57.46	12.56	±0.52 K
T17	38.77	8.55	±0.56 K	53.16	12.85	±0.53 K
T18	37.59	8.32	±0.55 K	48.33	12.03	±0.50 K
T19	37.85	7.96	±0.52 K	41.78	10.09	±0.42 K
T20	38.41	8.75	±0.56 K	35.57	8.11	±0.34 K
Vacuum manometer	13.32	4.39	±0.88 kPa	18.28	6.67	±1.34 kPa

result (R^2 = 0.51) compared to three times. Besides, R^2 values of the copper *TPCT* were calculated as 0.69 and 0.71, while the values of glass *TPCT* were obtained as 0.89 and 0.91 at 120th and 180th seconds, respectively. On the other hand, the maximum *RMSE* value was obtained as 10.26 at 60th second for the glass *TPCT*, while the minimum *RMSE* value was acquired as 4.09 at 120th second for copper *TPCT*. The measurement devices' technical properties and the average of the measured values, standard deviation, and the uncertainty for copper and glass *TPCTs* were given in Tables 4 and 5, respectively.

According to Table 5, the maximum *U* was obtained as ±0.56 K at T17 in glass *TPCT* while the minimum *U* was obtained as ±0.25 K at T2 in copper *TPCT*. Besides, *U* of vacuum manometer was calculated as ±0.88 kPa and ±1.34 kPa in copper and glass *TPCTs*, respectively.

3.2. Parametric numerical results of TPCT

k–ε turbulence model, which is used in the most general multiphase turbulence, was applied in both *VOF* and Eulerian multiphase models. Nevertheless, different turbulence models like *LES, k-kl ω* transition, *k-ω, SAS*, and *Re-Stress* with *k–ε* were examined in *VOF,* which have more turbulence options than Eulerian for comparing them. The average *CFD* temperature and all thermocouples change for the evaporation, middle and condensation regions in the glass *TPCT* for different turbulence models was given in Fig. 15.

According to Fig. 15a and b, the average *CFD* temperatures for *SAS*, *k–ε*, and *Re-Stress* turbulence models showed a similar trend to each other for *VOF* model. In case of comparison of the average temperature values in the maximum ΔT_{abs} values were calculated as 12.09 K, 21.73 K, 17.97 K, 15.41 K, 14.73 K, and 14.17 K for *LES*, *k-kl ω* transition, *k-ω*, *SAS*, *k–ε*, and *Re-Stress* turbulence models, respectively in the middle region. On the other hand, the maximum ΔT_{abs} values were calculated as 22.26 K, 26.07 K, 22.11 K, 22.84 K, 21.80 K, and 21.63 K for *LES*, *k-kl ω* transition, *k-ω*, *SAS*, *k–ε*, and *Re-Stress* turbulence models, respectively in considering all thermocouples. ΔT_{abs} values between experimental and different turbulence model results in the glass *TPCT* for the end of *VOF* model was given in Table 6.

According to Table 6, the ΔT_{abs} values for different turbulence model results have changed as different values which close some of experimental results and far from them. The minimum ΔT_{abs} value was calculated as 0.41 K for *k-ω* turbulence model in T17 while the maximum ΔT_{abs} value was found as 26.07 K for *k-kl ω* transition turbulence model in T7. The numerical temperature change at the end of the analysis for the regions and some thermocouples in the copper *TPCT* in *Eulerian* model for the different heat powers was given in Fig. 16.

According to Fig. 16a, the average temperature values for the evaporation region have increased with rising heat power of that while the other average temperatures have shown similar values. According to Fig. 16b, the numerical temperature values of T1 for 100 W, 150 W, 200 W, and 250 W were obtained as 337.67 K, 344.48 K, 351.56 K, and 358.18 K, respectively. Besides, the numerical temperature values of T6 for the same heating powers were obtained as 328.82 K, 330.13 K, 333.65 K, and 339.65 K, respectively. On the other hand, the numerical temperature values of T15 for the same heating powers were obtained as 322.05 K, 323.34 K, 324.34 K, and 325.28 K, respectively. Also, the numerical temperature contours at the end of the analysis in the copper *TPCT* in *Eulerian* model for the different heat powers was given in Fig. 17. According to Fig. 17, the numerical temperature contours for different heat powers have showed similar trend with different temperature values.

The experimental thermal resistance values were given in our previous study [38]. The thermal resistance (*R*) of the copper *TPCT* in *Eulerian* model calculated at the different (a) heat powers, (b) liquid volumes, and (c) inclination angles for *CFD* results was given in Fig. 18.

According to Fig. 18a, *R* values have rapidly decreased up to 150 W and then slowly decreased to 200 W and 250 W. The numerical *R* values were calculated as 0.1516, 0.1373, 0.1338, and 0.1322 while the experimental *R* values were found as 0.0977, 0.0792, 0.0793, and 0.0771 for the heating powers of 100 W, 150 W, 200 W, and 250 W, respectively. On the other hand, the numerical *R* values have slowly increased up to the liquid volume of 20 ml while the numerical *R* values have shown the fluctuations in Fig. 18b. The numerical *R* values were

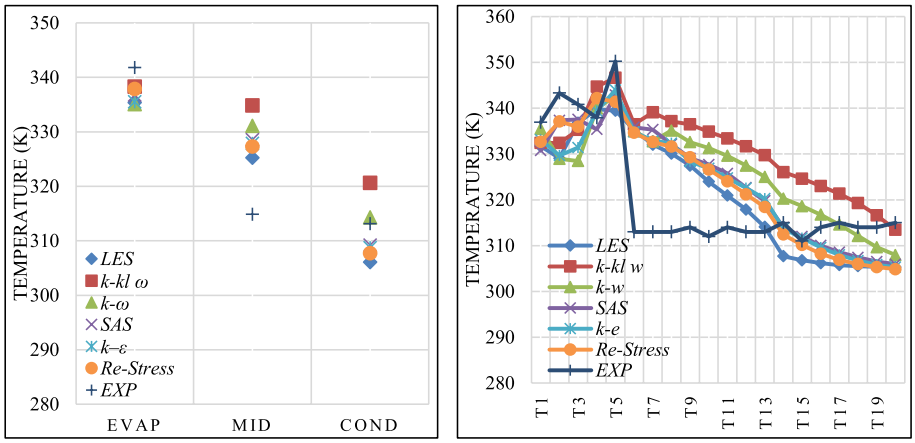

a b

Fig.15. The (a) average *CFD* temperature and (b) all thermocouples change for the evaporation, middle and condensation regions in glass *TPCT* for different turbulence models.

Table 6
ΔT_{abs} values between experimental and different turbulence model results in the glass *TPCT* for the end of *VOF* model.

Thermocouples	$\Delta T_{abs}(\pm K)$					
	LES	*k-kl ω*	*k-ω*	*SAS*	*k–ε*	*Re-Stress*
T1	5.21	4.47	1.42	6.14	3.80	4.28
T2	14.25	10.91	14.36	5.97	13.63	6.20
T3	3.98	5.55	12.32	3.25	9.40	4.86
T4	1.84	6.79	2.05	2.54	1.48	4.25
T5	10.76	3.58	7.55	7.36	6.23	8.81
T6	22.26	23.50	21.98	22.84	21.80	21.63
T7	19.05	26.07	19.73	22.32	19.89	19.62
T8	17.09	24.13	22.11	19.13	19.34	18.60
T9	13.48	22.44	18.57	15.08	14.34	15.27
T10	11.96	22.85	19.30	15.68	14.88	14.62
T11	6.95	19.39	15.61	11.76	10.79	10.02
T12	4.89	18.70	14.45	9.64	9.56	8.20
T13	1.10	16.75	12.00	6.80	7.25	5.41
T14	7.30	11.02	5.29	0.99	1.25	2.57
T15	4.18	13.61	7.63	0.96	0.66	0.84
T16	7.82	9.03	2.76	3.96	4.40	5.76
T17	9.25	6.32	0.41	6.43	7.02	8.12
T18	8.48	5.27	1.88	6.56	7.25	8.03
T19	8.62	2.63	4.34	7.47	8.15	8.68
T20	9.69	1.53	7.04	9.06	9.71	10.13

found as 0.1117, 0.1120, 0.1132, and 0.1154 while the experimental of that were calculated as 0.1165, 0.0854, 0.1029, and 0.0912 for the liquid volume of 5 ml, 10 ml, 15 ml, and 20 ml, respectively. Beside these, *R* values have continuously decreased from the inclination angle of 30° to 90° at the constant heating power of 100 W. The numerical *R* values were calculated as 0.1665, 0.1570, 0.1542, and 0.1516 while the experimental *R* values were found as 0.1603, 0.1140, 0.0948, and 0.0895 for the inclination angles of 30°, 45°, 60°, and 90°, respectively, as shown in Fig. 18c. As the numerical results compared the experimental results [38], the minimum deviations observed between *EXP* and *CFD* analysis were 55.24%, 4.06%, and 3.84% for different heat powers, liquid volumes, and inclination angles, respectively.

4. Conclusions

In this study, a comprehensive experimental and numerical study was performed for the glass and copper *TPCT's* thermal performance analysis in detail. A new combined numerical model of the *TPCT* was composed of 3D and analyzed thermodynamically using ANSYS Fluent 15 software. *VOF* model has been used for the first 60 s, and Eulerian model has been employed after 60 s until 180 s for the first time in the literature. The experimental and numerical results were also compared with each other in real-time steps for the first time in the literature. Although the glass *TPCT* was used to observe the boiling process in the *TPCT*, the thermal performance of that was investigated.

The main results of this comprehensive study are given as:

1. The maximum ΔT_{abs} of the evaporation, middle and condenser regions for glass *TPCT* are 9.09 K at 5th second, 18.63 K at 30th second, and 6.81 K at 80th second, respectively. On the other hand, these values for copper *TPCT* are calculated as 10.30 K at 5th second, 8.64 K at 25th second, and 7.74 K at 5th second, respectively.
2. The statistical values, which are calculated in a few studies in the literature, belonging to 60th second, showed the best result (R^2 = 0.93) for copper *TPCT*. In contrast, the statistical values belonging to 180th second demonstrated the best result (R^2 = 0.91) for glass *TPCT*.
3. As different from the literature, the steam volume of *TPCTs* is zero at the beginning of the analysis as in reality. The boiling was performed as the core bubbles and vapor slug until 25th second. After this time, the boiling process slowed down, but the geyser boiling occurred with pulsating at some time, such as 40th second.
4. The maximum *U* was obtained as ±0.56 K at T17 in a glass *TPCT*, while the minimum *U* was obtained as ±0.25 K at T2 in copper *TPCT*. Besides, *U* in vacuum manometer was calculated as ±0.88 kPa and ±1.34 kPa in glass and copper *TPCTs*, respectively.
5. The maximum ΔT_{abs} values were calculated between 12.09 K and 26.07 K for different turbulence models.
6. *R* values have rapidly decreased up to 150 W and then slowly decreased to 200 W and 250 W. On the other hand, the numerical *R* values have slowly increased up to the liquid volume of 20 ml while the numerical *R* values have shown fluctuations. Beside these, *R* values have continuously decreased from the inclination angle of 30° to 90° at the constant heating power of 100 W.

The temperature distributions on the surface of the *TPCTs* and the steam volume variation inside the glass *TPCT* have shown a similar trend with the studies in the literature. In a comparison of these results with similar studies in the literature, the maximum ΔT_{abs} values in the evaporation, middle, and condenser regions for *TPCT* ranged from 6.81 K and 18.63 K, and these values are similar with the values being between 15.94 K and 42 K in the other studies [21] from the literature. On the other hand, this comprehensive study carried out the new combined numerical analysis of the *TPCT* will provide significant contribution to the literature. Furthermore, the development of the numerical analysis

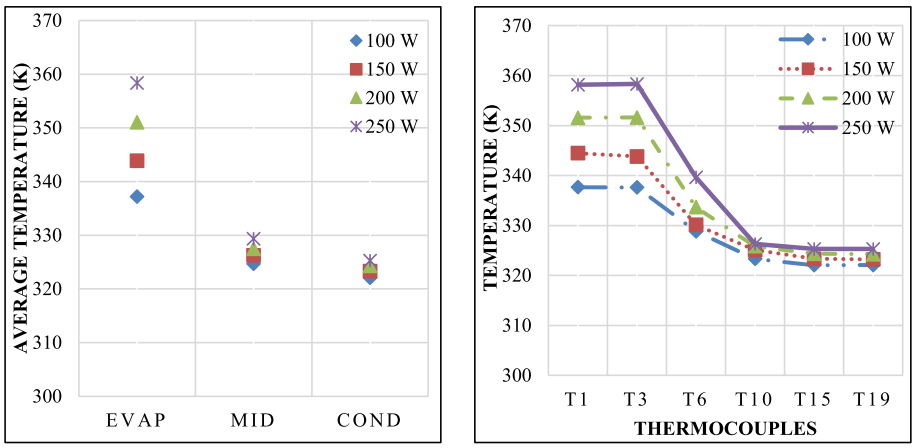

Fig. 16. The numerical temperature change of end of the analysis for (a) the regions (b) some thermocouples in the copper *TPCT* in *Eulerian* model for the different heat powers.

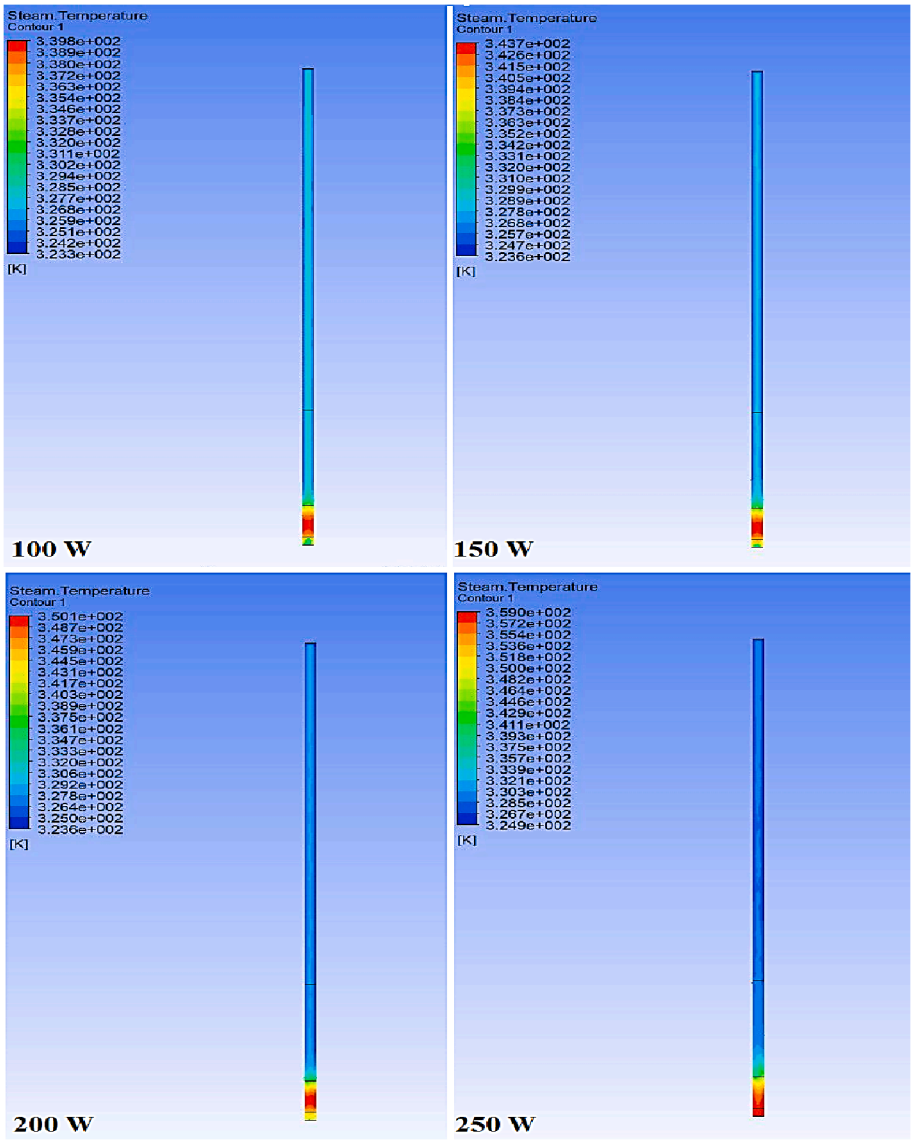

Fig. 17. The numerical temperature contours at end of the analysis in the copper *TPCT* in *Eulerian* model for the different heat powers.

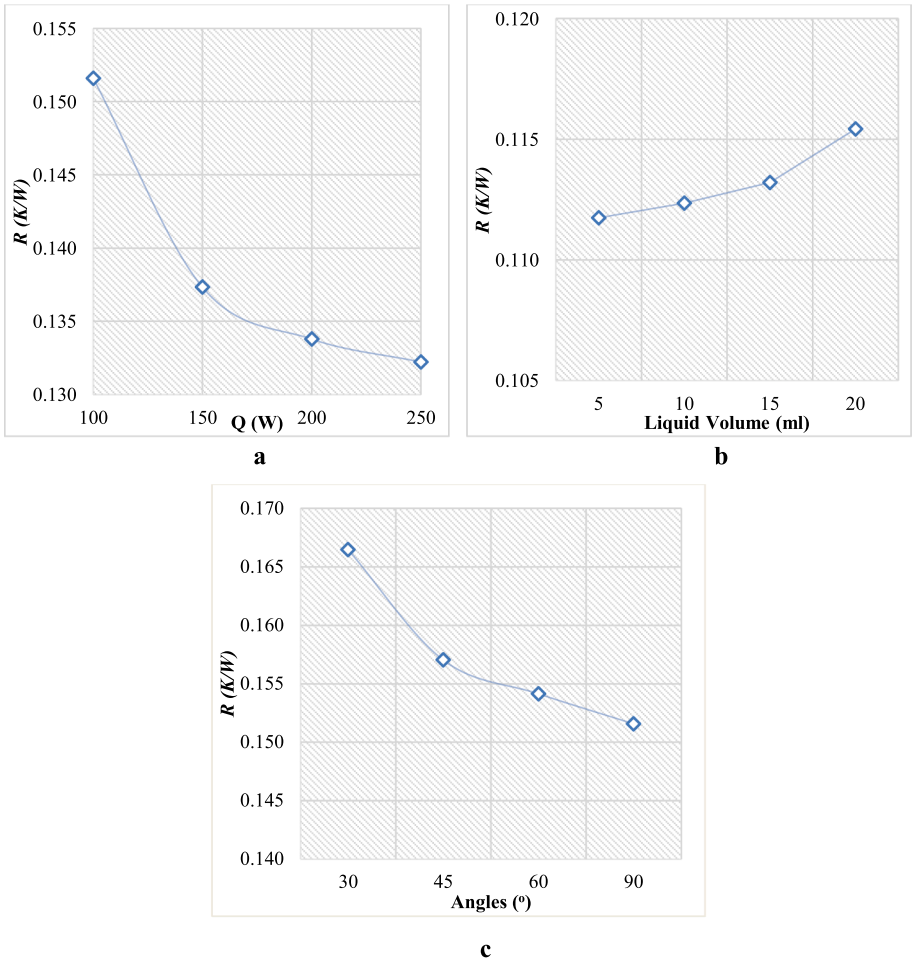

Fig. 18. *R* of the copper *TPCT* in *Eulerian* model calculated at the different (a) heat powers, (b) liquid volumes, and (c) inclination angles for *CFD* results.

will continue as a parametric study in detail.

CRediT authorship contribution statement

Halit Arat: Conceptualization, Methodology, Software, Validation, Investigation, Resources, Data curation, Writing - original draft, Writing - review & editing, Visualization. **Oguz Arslan:** Conceptualization, Methodology, Writing - original draft, Writing - review & editing, Visualization, Supervision. **Umran Ercetin:** Conceptualization, Methodology, Writing - review & editing, Software, Formal analysis, Supervision. **Abdullah Akbulut:** Conceptualization, Methodology, Writing - review & editing, Visualization, Supervision.

Declaration of Competing Interest

The authors declare that they have no known competing financial interests or personal relationships that could have appeared to influence the work reported in this paper.

Acknowledgments

This study was supported by Kutahya Dumlupinar University Scientific Research Projects Unit (DPU-BAP) under the grant of the project number of 2017-55.

Halit Arat, 1st author, would like to thank Technological Research Council of Turkey, National Scholarship Program for Ph.D. students (TUBITAK-BIDEB) for its financial assistance during his doctoral studies.

References

[1] D. Schneider, M. Lauer, I. Voigt, W.G. Drossel, Development and examination of switchable heat pipes, Appl. Therm. Eng. 99 (2016) 857–865, https://doi.org/10.1016/j.applthermaleng.2016.01.086.

[2] H. Arat, O. Arslan, Exergoeconomic analysis of district heating system boosted by the geothermal heat pump, Energy. 119 (2017) 1159–1170, https://doi.org/10.1016/j.energy.2016.11.073.

[3] S. Rashidi, O. Mahian, E.M. Languri, Applications of nanofluids in condensing and evaporating systems: A review, J. Therm. Anal. Calorim. 131 (3) (2018) 2027–2039, https://doi.org/10.1007/s10973-017-6773-7.

[4] M. Senturk Acar, O. Arslan, Energy and exergy analysis of solar energy-integrated, geothermal energy-powered Organic Rankine Cycle, J. Therm. Anal. Calorim. 137 (2) (2019) 659–666, https://doi.org/10.1007/s10973-018-7977-1.

[5] D. Sun, J. Xu, Q. Chen, Modeling of the evaporation and condensation phase-change problems with FLUENT, Numer. Heat Transf. Part B Fundam. 66 (4) (2014) 326–342, https://doi.org/10.1080/10407790.2014.915681.

[6] Y. Tang, S.-L. Zhu, L.-M. Qiu, Determination of mass transfer coefficient for condensation simulation, Int. J. Heat Mass Transf. 143 (2019) 118485, https://doi.org/10.1016/j.ijheatmasstransfer.2019.118485.

[7] C.R. Kharangate, I. Mudawar, Review of computational studies on boiling and condensation, Int. J. Heat Mass Transf. 108 (2017) 1164–1196, https://doi.org/10.1016/j.ijheatmasstransfer.2016.12.065.

[8] B. Nichita, J. Thome, A level set method and a heat transfer model implemented into FLUENT for modeling of microscale two phase flows, 178 Spec, Meet. Syst, Lev, 2010.

[9] A.W. Badar, R. Buchholz, F. Ziegler, Single and two-phase flow modeling and analysis of a coaxial vacuum tube solar collector, Sol. Energy. 86 (1) (2012) 175–189, https://doi.org/10.1016/j.solener.2011.09.021.

[10] T. Tsutsumi, S. Takeuchi, T. Kajishima, Heat transfer and particle behaviours in dispersed two-phase flow with different heat conductivities for liquid and solid, in: Flow, Turbul. Combust., Springer, 2014: pp. 103–119. https://doi.org/10.1007/s10494-013-9498-0.

[11] L. Lu, H. Liao, X. Liu, Y. Tang, Numerical analysis on thermal hydraulic performance of a flat plate heat pipe with wick column, Heat Mass Transf. Und Stoffuebertragung. 51 (8) (2015) 1051–1059, https://doi.org/10.1007/s00231-014-1475-1.

[12] S. Kakaç, A. Pramuanjaroenkij, Analysis of Convective Heat Transfer Enhancement by Nanofluids: Single-Phase and Two-Phase Treatments, J. Eng. Phys. Thermophys. 89 (3) (2016) 758–793, https://doi.org/10.1007/s10891-016-1437-1.
[13] Y. Gao, Y. Cui, B. Xu, B. Sun, X. Zhao, H. Li, L. Chen, Two phase flow heat transfer analysis at different flow patterns in the wellbore, Appl. Therm. Eng. 117 (2017) 544–552, https://doi.org/10.1016/j.applthermaleng.2017.02.058.
[14] O. Hamouda, D.S. Weaver, J.R. Riznic, Transient two-phase blowdown: Experiments and analysis, Int. J. Multiph. Flow. 104 (2018) 307–321, https://doi.org/10.1016/j.ijmultiphaseflow.2018.01.002.
[15] A. Wlazlak, B. Zajaczkowski, M. Woluntarski, M.H. Buschmann, Influence of graphene oxide nanofluids and surfactant on thermal behaviour of the thermosyphon, J. Therm. Anal. Calorim. 136 (2) (2019) 843–855, https://doi.org/10.1007/s10973-018-7632-x.
[16] K. Lim, J. Lee, 1-D two-phase flow analysis for interlocking double layer counter flow mini-channel heat sink, Int. J. Heat Mass Transf. 135 (2019) 305–317, https://doi.org/10.1016/j.ijheatmasstransfer.2019.01.092.
[17] D.R. Kaushal, T. Thinglas, Y. Tomita, S. Kuchii, H. Tsukamoto, CFD modeling for pipeline flow of fine particles at high concentration, Int. J. Multiph. Flow. 43 (2012) 85–100, https://doi.org/10.1016/j.ijmultiphaseflow.2012.03.005.
[18] A. Alizadehdakhel, M. Rahimi, A.A. Alsairafi, CFD modeling of flow and heat transfer in a thermosyphon, Int. Commun. Heat Mass Transf. 37 (3) (2010) 312–318, https://doi.org/10.1016/j.icheatmasstransfer.2009.09.002.
[19] Guerrero, F. Muñoz, N. Ratkovich, Comparison between eulerian and vof models for two-phase flow assessment in vertical pipes, CTyF - Ciencia, Tecnol. y Futur. 7 (2017) 73–84. https://doi.org/10.29047/01225383.66.
[20] S.C.K. De Schepper, G.J. Heynderickx, G.B. Marin, Modeling the evaporation of a hydrocarbon feedstock in the convection section of a steam cracker, Comput. Chem. Eng. 33 (1) (2009) 122–132, https://doi.org/10.1016/j.compchemeng.2008.07.013.
[21] B. Fadhl, L.C. Wrobel, H. Jouhara, Numerical modelling of the temperature distribution in a two-phase closed thermosyphon, Appl. Therm. Eng. 60 (1-2) (2013) 122–131, https://doi.org/10.1016/j.applthermaleng.2013.06.044.
[22] Z. Yang, X.F. Peng, P. Ye, Numerical and experimental investigation of two phase flow during boiling in a coiled tube, Int. J. Heat Mass Transf. 51 (5-6) (2008) 1003–1016, https://doi.org/10.1016/j.ijheatmasstransfer.2007.05.025.
[23] C. Gorlé, H. Lee, F. Houshmand, M. Asheghi, K. Goodson, P.R. Parida, Validation study for VOF simulations of boiling in a microchannel, in: ASME 2015 Int. Tech. Conf. Exhib. Packag. Integr. Electron. Photonic Microsystems, InterPACK 2015, Collocated with ASME 2015 13th Int. Conf. Nanochannels, Microchannels, Minichannels, 2015. https://doi.org/10.1115/IPACK2015-48129.
[24] J. Venkata Suresh, P. Bhramara, CFD Analysis of Multi turn Pulsating Heat pipe, in: Mater. Today Proc., Elsevier Ltd, 2017: pp. 2701–2710. https://doi.org/10.1016/j.matpr.2017.02.146.
[25] M.R.S. Emami, S.H. Noie, M. Khoshnoodi, M.T.H. Mosavian, A. Kianifar, Investigation of Geyser Boiling Phenomenon in a Two-Phase Closed Thermosyphon, Heat Transf. Eng. 30 (5) (2009) 408–415, https://doi.org/10.1080/01457630802414979.
[26] D. Zhang, H. Tao, M. Wang, Z. Sun, C. Jiang, Numerical simulation investigation on thermal performance of heat pipe flat-plate solar collector, Appl. Therm. Eng. 118 (2017) 113–126, https://doi.org/10.1016/j.applthermaleng.2017.02.089.
[27] G. Xia, W. Wang, L. Cheng, D. Ma, Visualization study on the instabilities of phase-change heat transfer in a flat two-phase closed thermosyphon, Appl. Therm. Eng. 116 (2017) 392–405, https://doi.org/10.1016/j.applthermaleng.2017.01.096.
[28] J.V. Suresh, P. Bhramara, CFD Analysis of Copper Closed Loop Pulsating Heat pipe, in: Mater. Today Proc., Elsevier Ltd, 2018: pp. 5487–5495. https://doi.org/10.1016/j.matpr.2017.12.138.
[29] K. Smith, R. Kempers, A.J. Robinson, Confinement and vapour production rate influences in closed two-phase reflux thermosyphons Part A: Flow regimes, Int. J. Heat Mass Transf. 119 (2018) 907–921, https://doi.org/10.1016/j.ijheatmasstransfer.2017.10.049.
[30] X. Wang, Y. Wang, H. Chen, Y. Zhu, A combined CFD/visualization investigation of heat transfer behaviors during geyser boiling in two-phase closed thermosyphon, Int. J. Heat Mass Transf. 121 (2018) 703–714, https://doi.org/10.1016/j.ijheatmasstransfer.2018.01.005.
[31] H. Jouhara, B. Fadhl, L.C. Wrobel, Three-dimensional CFD simulation of geyser boiling in a two-phase closed thermosyphon, Int. J. Hydrogen Energy. 41 (37) (2016) 16463–16476, https://doi.org/10.1016/j.ijhydene.2016.02.038.
[32] C. Kunkelmann, P. Stephan, CFD simulation of boiling flows using the volume-of-fluid method within OpenFOAM, Numer. Heat Transf. Part A Appl. 56 (8) (2009) 631–646, https://doi.org/10.1080/10407780903423908.
[33] J.U. Brackbill, D.B. Kothe, ScienceDirect - Journal of Computational Physics : A continuum method for modeling surface tension*1, J. Comput. Phys. 335354 (1992).
[34] W. Du, L. Zhang, S. Lv, P. Lu, J. Xu, W. Wei, Numerical study of liquid coverage in a gas-liquid-solid packed bed, Particuology. 23 (2015) 90–99, https://doi.org/10.1016/j.partic.2014.10.013.
[35] A.J. Le Fevre, E. J., Ede,, Laminar free convection from the outer surface of a vertical circular cylinder, Proc. 9th Int. Congr. Appl. Mech. 4 (1956) 175–183.
[36] A. Bejan, Convection Heat Transfer: Fourth Edition (2013), https://doi.org/10.1002/9781118671627.
[37] Y.A. Cengel, M.A. Boles, Thermodynamics: an Engineering Approach 5th Edition (2012).
[38] Halit Arat, Oguz Arslan, Umran Ercetin, Abdullah Akbulut, Experimental study on heat transfer characteristics of closed thermosyphon at different volumes and inclination angles for variable vacuum pressures, Case Stud, Therm. Eng. 26 (2021) 101117, https://doi.org/10.1016/j.csite.2021.101117.
[39] NIST Reference Database, REFPROP 9 (2010).
[40] D. Reay, P. Kew, Heat Pipes Theory, Design and Application, Fifth Edit, Butterworth-Heinemann, Elsevier, Oxford, 2006.
[41] Z.-H. Liu, Y.-Y. Li, R. Bao, Compositive effect of nanoparticle parameter on thermal performance of cylindrical micro-grooved heat pipe using nanofluids, Int. J. Therm. Sci. 50 (4) (2011) 558–568, https://doi.org/10.1016/j.ijthermalsci.2010.11.013.
[42] T.-H. Shih, W.W. Liou, A. Shabbir, Z. Yang, J. Zhu, A new k-∈ eddy viscosity model for high reynolds number turbulent flows, Comput. Fluids. 24 (3) (1995) 227–238, https://doi.org/10.1016/0045-7930(94)00032-T.
[43] D.C. Wilcox, Turbulence Modeling for CFD (1998).
[44] A. Guardo, M. Coussirat, M.A. Larrayoz, F. Recasens, E. Egusquiza, Influence of the turbulence model in CFD modeling of wall-to-fluid heat transfer in packed beds, Chem. Eng. Sci. 60 (6) (2005) 1733–1742, https://doi.org/10.1016/j.ces.2004.10.034.
[45] F.R. Menter, Review of the shear-stress transport turbulence model experience from an industrial perspective, Int. J. Comut. Fluid Dyn. 23 (4) (2009) 305–316, https://doi.org/10.1080/10618560902773387.
[46] H. Arat, Numerical Investigation of Heat Transfer of the Enclosures with Circular Cross-Section at the Vacuum Pressures: Designing of a New Solar Collector, Kutahya Dumlupinar University, 2021.
[47] M. Senturk Acar, O. Arslan, Performance analysis of a new hybrid cooling–drying system, Environ. Prog. Sustain. Energy. 37 (5) (2018) 1808–1828, https://doi.org/10.1002/ep.v37.510.1002/ep.12832.
[48] H. Arat, O. Arslan, Optimization of district heating system aided by geothermal heat pump: A novel multistage with multilevel ANN modelling, Appl. Therm. Eng. 111 (2017) 608–623, https://doi.org/10.1016/j.applthermaleng.2016.09.150.
[49] O. Arslan, ANN-based Determination of Optimum Working Conditions of Residential Combustors with Respect to Optimum Insulation, Energy Sources, Part A Recover. Util. Environ. Eff. 36 (23) (2014) 2603–2612, https://doi.org/10.1080/15567036.2011.572133.